Vertical gate-defined double quantum dot in a strained germanium double quantum well

Hanifa Tidjani,[1,*,‡] Alberto Tosato,[1,‡] Alexander Ivlev,[1] Corentin Déprez,[1] Stefan Oosterhout,[2] Lucas Stehouwer,[1] Amir Sammak,[2] Giordano Scappucci,[1] and Menno Veldhorst[1,†]

[1] *QuTech and Kavli Institute of Nanoscience, Delft University of Technology, P.O. Box 5046, Delft 2600 GA, The Netherlands*

[2] *QuTech and Netherlands Organisation for Applied Scientific Research (TNO), Delft, The Netherlands*

(Received 23 May 2023; revised 8 September 2023; accepted 2 October 2023; published 16 November 2023)

Gate-defined quantum dots in silicon-germanium heterostructures have become a compelling platform for quantum computation and simulation. Thus far, developments have been limited to quantum dots defined in a single plane. Here, we propose to advance beyond planar systems by exploiting heterostructures with multiple quantum wells. We demonstrate the operation of a gate-defined double quantum dot in a strained germanium double quantum well, where both quantum dots are tunnel coupled to both reservoirs and parallel transport occurs. We analyze the capacitive coupling to nearby gates and find both quantum dots to be accumulated under the central plunger gate. We extract their position and size, from which we conclude that the double quantum dots are vertically stacked in the two quantum wells. We discuss the challenges and opportunities of multilayer devices and outline some potential applications in quantum computing and quantum simulation.

DOI: 10.1103/PhysRevApplied.20.054035

I. INTRODUCTION

Semiconductor heterostructures composed of silicon and germanium have become the leading material platform for building quantum dot qubits [1–3]. Developments in their fabrication and operation have enabled demonstrations of high-fidelity single and two-qubit logic, multiqubit operation, and rudimentary quantum error correction [1,2,4–9]. Efforts in scaling quantum dots have led to the operation of a crossbar array comprising 16 quantum dots [10] and long-range quantum links may enable interconnecting modules of quantum dot arrays [11–14]. These developments in gate-defined quantum dots have been restricted to quantum dots defined in a single plane, yet the versatile nature of silicon-germanium heterostructures allows for further exploration. In particular, structures with multiple quantum wells can be grown and double quantum wells of germanium [15] and silicon [16,17] have been realized. An open question is thus whether multilayer heterostructures can become a relevant platform for quantum information. Here, we motivate potential applications and experimentally explore quantum dots in stacked quantum wells.

Heterostructures with parallel quantum wells may support integration of important functionalities for spin-qubit-based quantum processors, as depicted in Fig. 1(a). Precise control over the growth of individual layers allows for the engineering of inter- and intralayer properties. When charges residing in separate quantum wells are capacitively coupled but have little to no tunnel coupling, charge sensors could be integrated into separate layers from the qubits that they sense. In an intermediate regime where the tunnel coupling is in the order of one to a few tens of gigahertz, coherent spin shuttling between the wells could be realized [18]. Consequently, one layer may serve as a quantum link for qubits defined in the other layer, e.g., by offering shuttling lanes that connect remote qubits [14,19]. In this regime, the second layer can also host dedicated ancilla qubits that aid in spin-to-charge conversion for initialization and readout. Tunnel-coupled quantum wells may also be used to develop novel qubit implementations such as vertical singlet-triplet qubits or flopping-mode spin qubits [20]. Moreover, the thickness and atomic composition of each quantum well may be tuned to optimize g-tensors [21] and spin-orbit interactions [22], in order to provide dedicated functionality. In addition, double quantum wells engineered to provide different g-tensors could be used to execute quantum gates on spin qubits by shuttling the qubit between quantum dots defined in the two quantum wells [18,23]. This would enable qubit control with base-band pulses, diminishing the need for high-power microwave electronics.

Quantum dots in multiple quantum wells may also present new opportunities for analog quantum simulation.

*h.tidjani@tudelft.nl

†m.veldhorst@tudelft.nl

‡These authors contributed equally to this work.

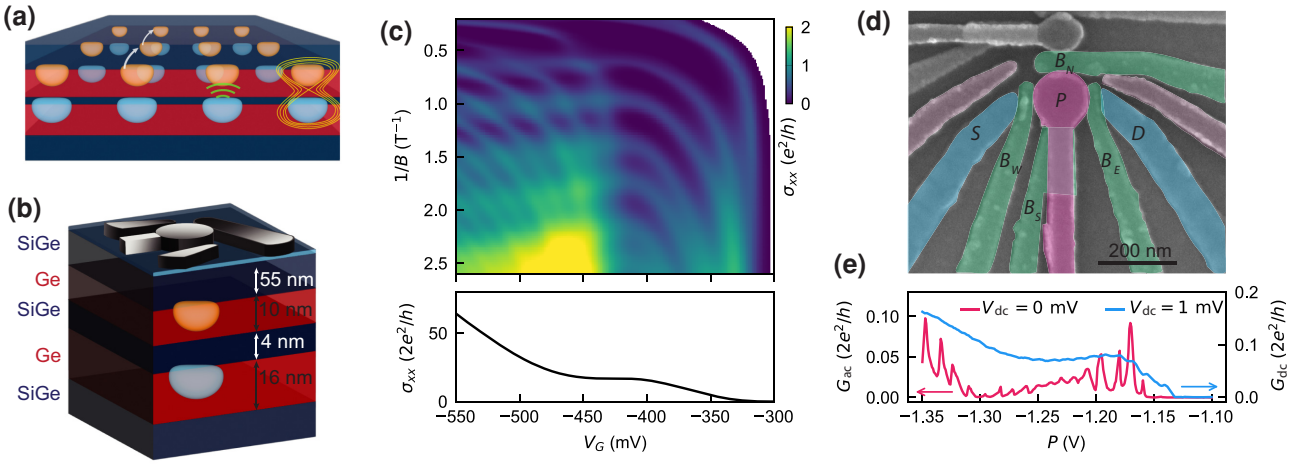

FIG. 1. Gate-defined vertical double quantum dot in a bilayer heterostructure. (a) A vision of a larger bilayer device, with different use cases depicted, such as shuttling (white), sensing (green), and vertical two-qubit gates (yellow). (b) Schematic of the heterostructure and gate stack. The light blue layer in between the gates and the SiGe layer indicates the aluminum oxide layer. (c) A color map of the conductivity σ_{xx} as a function of the gate voltage V_G and the inverse magnetic field $1/B$. The dark regions correspond to filled Landau levels with vanishing σ_{xx} and correspondingly quantized σ_{xy}. The lower panel shows a line cut at $B = 0$ T showing the zero-field conductance trace. The density and mobility for the bilayer system are presented in Appendix B. (d) A false-colored SEM image of a device that is nearly identical to the one used in this work. Quantum dots are defined under the plunger gate P (pink) and measured in transport using the Ohmic contacts source (S) and drain (D) (blue). The coupling between the quantum dot and the Ohmics is tuned by B_E and B_W (green). The potential landscape is further shaped by the gates B_N and B_S (green). The experiments presented in this work are performed on a section of a larger device (see Appendix C). (e) A conductance trace as a function of the plunger gate voltage across S-D at $V_{dc} = 1$ mV (blue line) and the differential conductance trace (pink) at $V_{dc} = 0$ mV and $V_{ac} = 17\ \mu$V, $f_{lock\text{-}in} = 70$ Hz.

While planar two-dimensional quantum dot arrays may be used to simulate correlated physics such as the resonating valence bond [24], quantum dots in a double quantum well may simulate even more exotic systems. For example, exciton condensation may be induced by the Coulomb interaction when the quantum dot occupation in one layer is almost filled and in the other is almost empty, creating an effective electron and hole layer. Such a gate-defined quantum dot system may provide more control over individual parameters when studying excitons, when compared to quantum transport implementations [25–28]. Quantum dots in multilayer structures comprised of three or more quantum wells could also be envisioned. The confinement of quantum dots in three layers potentially supports artificial superconductivity. Attractive Coulomb interaction in quantum dot systems has been observed in planar systems [29,30] and the integration of such interactions into a trilayer system may provide a route toward tunable and controllable superconducting condensation.

These motivations warrant the study of quantum dots defined in multilayer heterostructures. However, there are also many challenges in the design and operation that need to be understood and overcome. We take a first step and demonstrate a gate-defined vertical double quantum dot in a strained germanium double quantum well heterostructure. Through quantum transport measurements, we obtain charge-stability diagrams consistent with two quantum dots coupled in parallel. We characterize the capacitive interaction of the quantum dots to the surrounding gates and determine their location. The size of one of the quantum dots is estimated through bias spectroscopy. Together, these findings point toward the formation of a double quantum dot vertically aligned under the same plunger gate.

II. METHODS AND RESULTS

An undoped and compressively strained Ge/(SiGe) double quantum well heterostructure is epitaxially grown on a 100-mm Si(100) substrate. A 55-nm-thick $Si_{0.2}Ge_{0.8}$ spacer separates the bilayer system from the gate stack. The top and bottom quantum wells in the bilayer are 10-nm and 16-nm thick, respectively and are separated by a 4-nm $Si_{0.2}Ge_{0.8}$ barrier [Fig. 1(b)]. We perform magnetotransport characterization of a Hall-bar-shaped heterostructure field-effect transistor to infer the energy spectrum of the hole bilayer. The conductance map in Fig. 1(c) reveals the emergence of two sets of Landau levels typical of such a bilayer system [15,31]. At $V_G \approx -320$ mV, the longitudinal conductivity σ_{xx} shows the first set of quantized Landau levels, corresponding to the subband localized in the bottom well. At $V_G \approx -400$ mV, the conductance curve at zero magnetic field [Fig. 1(c), bottom panel] deviates from a linear increase and flattens out as the subband localized in the top well starts to be populated. This originates

from the electric field screening caused by the accumulation of charge carriers in the top well, while its density is still below the percolation threshold and transport is only available through the bottom well [15]. For more negative voltages, the carriers in the top well start to contribute to transport and the conductance increases. This confirms that this heterostructure is compatible with the accumulation of a bilayer 2D hole gas.

We then fabricate gates to electrostatically define quantum dots in this bilayer system (see Appendix A). A three-dimensional schematic depicting the heterostructure and gate stack and a scanning-electron-microscopy (SEM) image of a nominally identical device are, respectively, shown in Figs. 1(b) and 1(d). The gate geometry is similar to that of quantum dot devices with a single quantum well [2]. The central plunger gate P is negatively biased to accumulate holes beneath it, while the barrier gates B_W and B_E are used primarily to tune the tunnel barrier to the Ohmic contacts (S and D). The gates B_N and B_S further shape the potential landscape without significantly affecting the tunnel barrier to the Ohmics. We measure the transport through the device with dc and low-frequency lock-in techniques (see Appendix A).

At high source-drain dc bias [$V_{\mathrm{dc}} = 1$ mV, Fig. 1(e), blue line] the conductance trace starts to increase as P is lowered and a transport channel opens. After a first increase, the conductance plateaus at $P = -1.2$ V, before showing a second increase in conductance indicating the opening of a second transport channel. We study this same phenomenon at low bias $V_{\mathrm{dc}} = 0$ mV and measure the differential conductance using a lock-in amplifier. The differential conductance trace $dI_{\mathrm{ac}}/dV_{\mathrm{ac}}$ (pink line) reveals the emergence of Coulomb peaks, which begin at -1.14 V. Interestingly, the Coulomb peaks show a decrease in amplitude between -1.2 V and -1.3 V, after which the amplitude increases again. We speculate that this decrease in amplitude is caused by an increased tunnel coupling to a second parallel quantum dot that may not yet be contributing to transport itself. If this second quantum dot has lower conductance, an increased wave-function amplitude in this second quantum dot would reduce the Coulomb peak height [32]. This wave function delocalization across two tunnel-coupled quantum wells has also been predicted by Schrödinger-Poisson simulations [15]. At lower voltages, the second quantum dot also starts to contribute to transport and Coulomb peaks reemerge. While the intermediate voltage gives rise to a complex gate-voltage dependence, the observation of a double turn-on suggests the presence of a second quantum dot.

To further investigate the quantum dots in this bilayer system, we map the charge-stability diagram as a function of the gate voltages applied on B_N and P, shown in Figs. 2(a) and 2(b). A distinct honeycomb pattern emerges, indicating the presence of a double quantum dot system [33]. This is confirmed by an overlaid electrochemical simulation of a double quantum dot coupled in parallel, which reproduces the location of the charge transitions (for details of the model, see Appendix E). In the region between $P = -1.32$ V and $P = -1.25$ V, we observe transport at every edge of this honeycomb, corresponding to the interdot charge transition and the two reservoir to quantum dot transitions.

To distinguish the interdot transitions from the reservoir transitions in the charge-stability diagram of Figs. 2(a) and 2(b), we measure the differential conductance as a function of V_{dc} and P. The bottom panel of Fig. 2(b) shows a set of Coulomb diamonds taken in the regime where $B_N = -0.15$ V (magenta line cut shown in the top panel). The transition lines that fall on this line cut corresponding to a signal at $V_{\mathrm{dc}} = 0$ mV in the lower panel are indicated by the four colored arrows. The transition lines indicated by the blue and orange arrows correspond to the edges of the Coulomb diamonds and are attributed to quantum dot to reservoir transitions. In contrast, the transition line indicated by the green arrow lies in the middle of a Coulomb diamond and a conductance peak is barely visible. This is the expected behavior for an interdot transition, where transport is only possible through cotunneling processes, such as elastic cotunneling [34], resulting in a faint conductance signal, only when the two quantum dots are in resonance. The unusual negative slope of the interdot transition is a result from both B_N and P predominantly coupling to the same quantum dot, corresponding to the orange transitions (see Appendix D). With the four identified transition lines as a reference, we map each transition line in the charge-stability diagram using the hexagonal pattern and slopes of the lines.

The presence of the two reservoir-transition lines (blue and orange) indicates that both quantum dots are connected in parallel to the Ohmic contacts. At the interdot transition line (green), series transport may occur. Since a simulated double quantum dot system fits our data well, we consider the formation of a triple quantum dot improbable. Such a triple quantum dot would produce pentagonal or heptagonal features [35], which we do not observe. We further exclude the possibility of a triple quantum dot, as that would require at least two of the three quantum dots to be located in the same quantum well and, as a result, have distinct lever arms to the surrounding gates, which we elaborate on further in the upcoming paragraphs. We observe just two distinct reservoir transitions and argue in the following paragraphs that these must correspond to vertically stacked quantum dots.

The behavior of this bilayer quantum dot system outside of the explored parameter regimes may have different characteristics. Above $P = -1.2$ V, we expect there are two quantum dots, with one or both of them contributing to transport. Below $P = -1.35$ V, the system allows for multiple scenarios. The increasing quantum dot size with occupancy may cause delocalization across the two

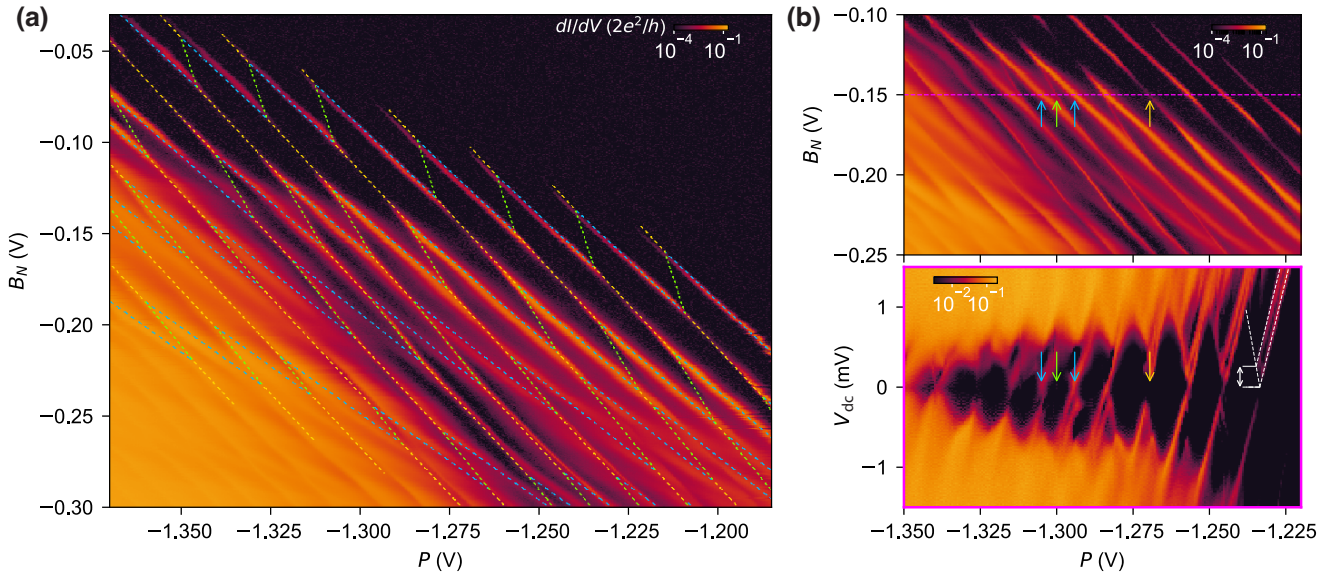

FIG. 2. Charge-stability diagram of the vertical double quantum dot. (a) By sweeping the gates P versus B_N, a honeycomb pattern emerges as the gates induce transport resonances. The dashed colored lines overlain on the data correspond to the electrochemical simulation of the double-quantum dot system, detailed in Appendix E. (b) The upper panel shows an enlargement of a subset of the data presented in (a), with colored arrows corresponding to different transitions. Lower panel bias spectroscopy across a line cut of the upper panel (magenta) at $B_N = -0.15$ V. The colored arrows correspond to the transitions highlighted in the upper panel. The measurement of the orbital energy for the first Coulomb diamond is indicated by the white lines and is extracted to be approximately 260 μeV. All measurements in this figure are acquired with a lock-in amplifier, with a typical frequency of 70 Hz and an amplitude of 17 μV.

quantum wells. High charge occupation may also result in a decreased charging energy and high coupling to the Ohmics, which can give rise to a constant background current, potentially observed in the bottom-left region of Fig. 2(a), if a dot opens to a channel. Additionally, a high top gate voltage may result in wave function localization in the top quantum well, resulting in only the top quantum dot contributing to transport.

Unlike a typical double-quantum dot charge-stability diagram [33] where each quantum dot predominantly responds to its own dedicated plunger gate, transition lines in this diagram have very similar slopes, indicating that the gates have similar lever-arm ratios α_{B_N}/α_P to both quantum dots. This observation is consistent with vertically stacked quantum dots of similar shape, as the lever-arm ratio primarily depends on the in-plane position of the quantum dots. Crucially, we are still able to populate both quantum dots, which is not trivial for a vertically coupled double quantum dot due to possible screening by the top well (see Appendix D). In this device, this is aided by a higher charging energy of the top dot resulting from increased confinement. On the other hand, the reduced confinement increases the size of the bottom quantum dot and hence its lever arm to the surrounding gates.

Next, we extract the position of both quantum dots using the measured capacitive coupling to the surrounding gates. We map the charge-stability diagram as a function of B_i $(i = N, W, S, E)$ and P (see Appendix Fig. 8) and based on the slopes of the reservoir transitions we find that both quantum dots have comparable lever arms to all surrounding gates [Fig. 3(a)]. A first observation is that both quantum dots are most strongly coupled to the plunger gate, giving a first indication that they are located underneath it. Importantly, we find that all barrier gates have a similar capacitive coupling to the quantum dots. The symmetry of this coupling suggests there are no spurious quantum dots, with the observed quantum dots both being located underneath the plunger gate. Additionally, we find that one quantum dot has a higher lever-arm ratio $\alpha_{B_i,D_i}/\alpha_{P,D_i}$ to all barrier gates. This is consistent with a stacked double quantum dot, where the top quantum dot is expected to be smaller, causing a reduction of the coupling to the barrier gates.

To further support the conclusion of having created a vertical double quantum dot, we estimate the position of both quantum dots using an electrostatic finite-element-method (FEM) simulation in ANSYS Q3D [36], in which the heterostructure, gate layers, and insulating layers are included (details can be found in Appendix G). The quantum dots are simulated individually in both layers, to analyze all their possible locations [Fig. 3(d)]. Each quantum dot is modeled as a metallic disk that is as thick as the quantum well in which it is located. The radius and position of this simulated metallic quantum dot are varied to

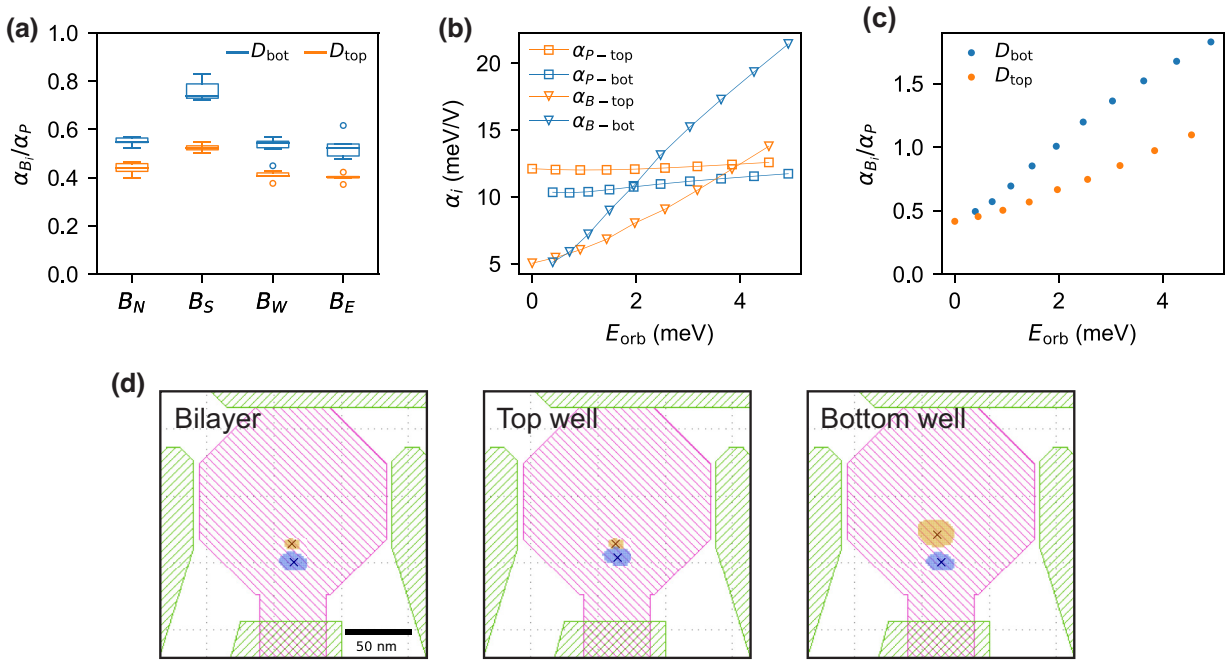

FIG. 3. The measured and simulated lever-arm ratios of the surrounding gates to the quantum dots and the triangulation of their center points. (a) A box plot of the lever-arm ratios ($\alpha_{B_i,D_i}/\alpha_{P,D_i}$) of each barrier gate B_i to the plunger gate P for the top and bottom quantum dot (D_i). These couplings are extracted from the slopes of different reservoir transitions in the charge-stability diagrams as a function of B_i and P (see Appendix E). The spread in $\alpha_{B_i,D_i}/\alpha_{P,D_i}$ for different occupations is small compared to the difference in $\alpha_{B_i,D_i}/\alpha_{P,D_i}$ between the two quantum dots, ensuring that the average value of $\alpha_{B_i,D_i}/\alpha_{P,D_i}$ for a quantum dot across a range of different occupations is a meaningful metric for assessing the positioning of the quantum dots with respect to the surrounding gates. (b) Simulated lever arms for the plunger gate P and barrier gate B to the top and bottom quantum dot calculated from the 2D Schrödinger-Poisson simulation described in Appendix F. (c) Simulated lever-arm ratios $\alpha_{B_i,D_i}/\alpha_{P,D_i}$ for the first 20 orbital states, plotted against the orbital energy (E_{orb}), with data extracted from the Schrödinger-Poisson simulation. (d) The triangulation of the position of the quantum dots by comparing the lever-arm ratios in (a) with capacitive simulation (Appendix G). The cross indicates the center point of each quantum dot and the colored area represents the 1σ standard deviation of this value. In the "Bilayer" panel, the quantum dots are simulated one at a time in separate wells, with the orange quantum dot and blue quantum dot placed in the top and bottom well, respectively. In the "Top well" and "Bottom well" panels, the quantum dots are simulated one at a time in the same layer.

analyze the effect on the capacitance. The geometric capacitance between each metallic quantum dot D and each gate G is determined and assumed to be directly proportional to the lever arm $\alpha_{G,D}$. By comparing the simulated capacitance with the measured lever-arm ratio $\alpha_{B_i,D}/\alpha_{P,D}$, the position of a single quantum dot within either quantum well is triangulated. The predicted center-to-center distance between the quantum dots has an upper bound of 30 nm [Fig. 3(d)], regardless of the well in which the quantum dots are simulated. This close proximity prohibits the coexistence of both quantum dots in the same layer without coalescing, suggesting that the quantum dots must be located in different quantum wells. We account for a 1σ error in the position, as indicated by the colored area in Fig. 3(d), which is based on the spread of the lever-arm ratios that are extracted from each charge-stability diagram.

We estimate the size of one quantum dot from the orbital energy $E_{orb} = 260$ μeV extracted from Fig. 2(b) (lower panel, white lines). Assuming a harmonic in-plane potential $V_{xy} = \frac{1}{2}m^*\omega^2(x^2+y^2)$, where $\hbar\omega = E_{orb}$ and $m^* = 0.055m_e$, this gives a quantum dot diameter of about $d = \sqrt{\hbar/(\omega m^*)} = 137$ nm, comparable to the plunger gate size of 150 nm. Based on the size approximation of this quantum dot and their mutual proximity, we conclude that the quantum dots cannot coexist in a single layer without coalescing. Overall, the measured lever-arm ratios, together with the results from the FEM simulation and the estimates of the quantum dot size from the Coulomb diamonds, provide strong arguments for the quantum dots being vertically stacked under the plunger gate.

To identify in which quantum well each quantum dot resides, we perform a 2D Schrödinger-Poisson simulation [Figs. 3(b) and 3(c)]. We calculate the capacitive coupling between the plunger gate P and a barrier gate B for consecutive orbital fillings of the top and bottom quantum dot to deduce the lever arms [Fig. 3(b)]. While the lever arm of the plunger gate to the top and bottom quantum dot (α_{P-top} and α_{P-bot}) remains approximately constant with increasing orbital number, the barrier gate

lever arm to both quantum dots varies significantly with the orbital number. This originates from an increase in the wave function spread for consecutive orbitals, increasing the overlap and consequently the coupling to the barrier gate. Figure 3(c) shows the corresponding lever-arm ratio of the quantum dots formed in the top quantum dot (D_{top}) and bottom quantum dot (D_{bot}) for different orbitals. The figure shows that for all simulated orbitals, the bottom quantum dot has a relatively larger lever arm to the barrier gates. Comparing this to the measured lever-arm ratios in Fig. 3(a), we conclude that D_{top} [orange transitions in Fig. 2(a)] corresponds to a quantum dot located in the upper quantum well and D_{bot} [blue transitions in Fig. 2(a)] to a quantum dot located in the bottom quantum well. This interpretation is confirmed by the position and slope of the interdot transitions in the charge-stability diagrams. As the plunger gate voltage becomes more negative, attracting holes to the gate, a hole tunnels from D_{bot} to D_{top} across the interdot transition. We therefore conclude that D_{top} is localized in the top well.

III. DISCUSSION AND OUTLOOK

In this work, we demonstrate a double quantum dot defined in a double quantum well heterostructure. A single gate can be used to simultaneously populate quantum dots in two wells, while the charge occupation can be tuned using one of the surrounding gates. From the double quantum dot charge-stability diagrams obtained from mapping P versus B_i, we extract the lever-arm ratios of the quantum dots to the surrounding gates and confirm that neither quantum dot couples strongly to a particular barrier gate, excluding the possibility of a spurious dot. By comparing the lever-arm ratios to an electrostatic FEM simulation, we triangulate the in-plane position of the quantum dots and find their center points at approximately the same in-plane position. If the quantum dots were to be in the same quantum well, we would expect a much larger coupling than observed and effectively a merged quantum dot. Furthermore, the estimated quantum dot diameter $D_{\text{bot}} = 137\,\text{nm}$ suggests that a double quantum dot can only exist by occupying both quantum wells. Based on these findings, we conclude the realization of a vertically coupled double quantum dot in a double quantum well.

The operation of many quantum dots, and specifically many vertical double quantum dots, is certainly not an easy task. However, we can envision that a set of plunger gates, barrier gates, and gates at the corners in a 2D array could jointly provide a virtual gate space to control the charge occupation in the quantum dots, as well as the lateral tunnel coupling between the quantum dots. In doing so, vertically coupled quantum dots may provide new means for scaling, coupling, and addressing semiconductor quantum dot qubits.

The raw data and analysis supporting the findings of this study are openly available in a Zenodo repository [37].

ACKNOWLEDGMENTS

We acknowledge useful discussions with members of the Veldhorst, Scappucci, and Vandersypen groups. We thank S. G. J. Philips and S. De Snoo for the development of the software stack used to acquire data in this experiment. We acknowledge support through a Dutch Research Council (NWO) Domain Science (ENW) grant and a European Research Council (ERC) Starting Grant QUIST (850641).

The authors declare no competing interests.

APPENDIX A: METHODOLOGICAL DETAILS

The device is fabricated on a Si_xGe_{1-x}/Ge/Si_xGe_{1-x}/Ge/Si_xGe_{1-x} heterostructure, where $x = 0.2$, grown by reduced-pressure chemical vapor deposition. The virtual substrate on which the heterostructure is grown consists of a silicon substrate, upon which there is a 1.6-μm relaxed Ge layer; a 1-μm graded Si_xGe_{1-x} layer, with a final Ge composition of $x = 0.2$. On top of the SiGe virtual substrate, the bilayer system comprises a 16-nm-thick bottom Ge quantum well, a 4-nm-thick SiGe barrier, a 10-nm-thick top Ge quantum well, and a final 55-nm-thick SiGe spacer. At the top of the stack, a sacrificial Si cap is grown to provide a native SiO_x layer. We define Ohmic contacts using electron-beam lithography and remove the Si cap in the exposed area using a buffered-oxide etch. We then evaporate a 30-nm platinum layer and contact the quantum wells using a 10-min rapid thermal anneal at 400 °C, forming platinum germanosilicides. The Ohmic layer is isolated using a 7-nm layer of Al_2O_3 grown by atomic layer deposition. The electrostatic gates used to define the quantum dots are patterned in two layers (3/17 nm and 3/37 nm of Ti/Pd) and are separated by a 5-nm layer of Al_2O_3.

The devices are screened in 4 K liquid helium. The experiments reported in this paper are carried out in a Bluefors LD400 dilution refrigerator with a base temperature of 10 mK. The electrical properties of the quantum dots are investigated through two-terminal ac and dc measurements. We apply a tunable dc bias V_{dc} across the source (S) and drain (D) and measure the resulting current with a Keysight digitizer; from this, we calculate the conductance $G_{\text{dc}} = I_{\text{dc}}/V_{\text{dc}}$. To measure differential conductance, we use a lock-in technique and apply a sinusoidal bias with frequency 70 Hz and amplitude $V_{\text{ac}} = 17\ \mu\text{V}$, from which we can calculate the differential conductance $G_{\text{ac}} = dI/dV = I_{\text{ac}}/V_{\text{ac}}$. When we acquire using the digitizer, the amplitude of the lock-in input signal is reduced to $V_{\text{ac}} = 0.04\ \mu\text{V}$.

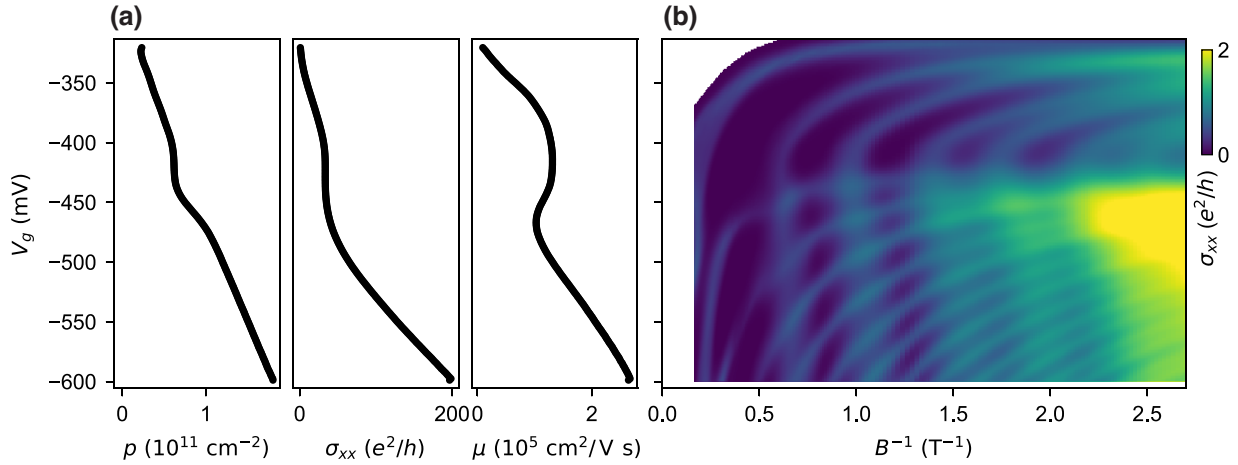

FIG. 4. The magnetotransport characterization of the hole bilayer measured using a Hall-bar-shaped field-effect transistor. (a) From left to right, the gate voltage (V_g) dependence of the hole-bilayer Hall density p, conductivity σ_{xx} at zero magnetic field, and mobility μ. (b) The color map of the conductivity σ_{xx} as a function of V_g and the inverse magnetic field B^{-1}. The dark regions correspond to filled Landau levels with vanishing σ_{xx} and correspondingly quantized σ_{xy}.

APPENDIX B: MAGNETOTRANSPORT

Figure 4(a) shows the magnetotransport characterization of a Hall-bar-shaped device. In the voltage range between −250 mV and −400 mV, only the bottom quantum well is occupied and the density shows a linear dependence on the gate voltage, while the mobility and conductivity increase monotonically. The fan diagram in Fig. 4(b) shows the typical pattern of single-channel transport. Below −400 mV, population of the top well becomes energetically favorable but its density remains below the percolation density until $V_G = -430$ mV, at which point it starts to contribute to transport. Any further increase in the electric field in the bottom well is screened by the charge added to the top well, leaving the bottom well density unchanged. Within the voltage region where the density in the bottom well remains constant and the holes added to the top well are not mobile, the bilayer density measured from the Hall effect plateaus, as do the conductivity and mobility. Beyond this region for $V_G < -430$ mV, the top quantum well is above the percolation threshold; hence charges are mobile and contribute to transport, resulting in a second set of Landau levels. While the bilayer density and conductivity increase with increasing negative voltages, the mobility curve drops before reestablishing its increasing trend. We ascribe this temporary drop in mobility to interlayer scattering [15].

APPENDIX C: FULL DEVICE

Figure 5 shows a false-colored SEM of the whole device, only the leftmost gates of which were used in this experiment.

APPENDIX D: DOUBLE QUANTUM DOT CHARGE-STABILITY DIAGRAMS FOR DIFFERENT SYSTEM PARAMETERS

The features of a double quantum dot charge-stability diagram strongly depend on the capacitive coupling between the gates and the quantum dots, as well as between the quantum dots themselves. These parameters are expected to be significantly different in a vertically coupled double quantum dot compared to more typical planar quantum dots. It is therefore instructive to qualitatively analyze the charge-stability diagram of a double

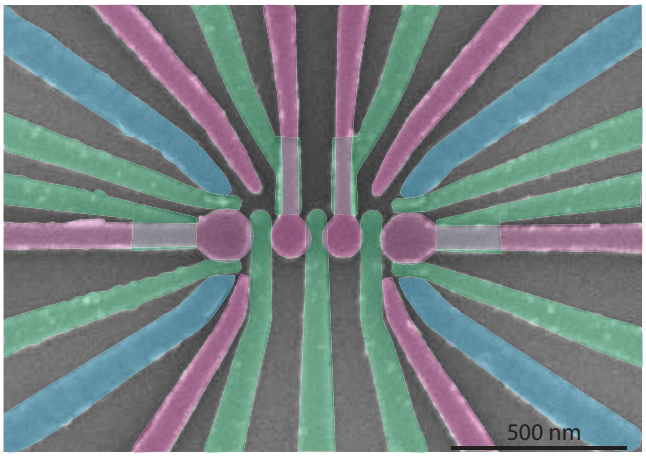

FIG. 5. A false-colored SEM of a device similar to the one used in this experiment. The experiments were conducted in quantum transport through the left quantum dot (purple) which is coupled to the Ohmics (blue) and controlled via barrier gates (green).

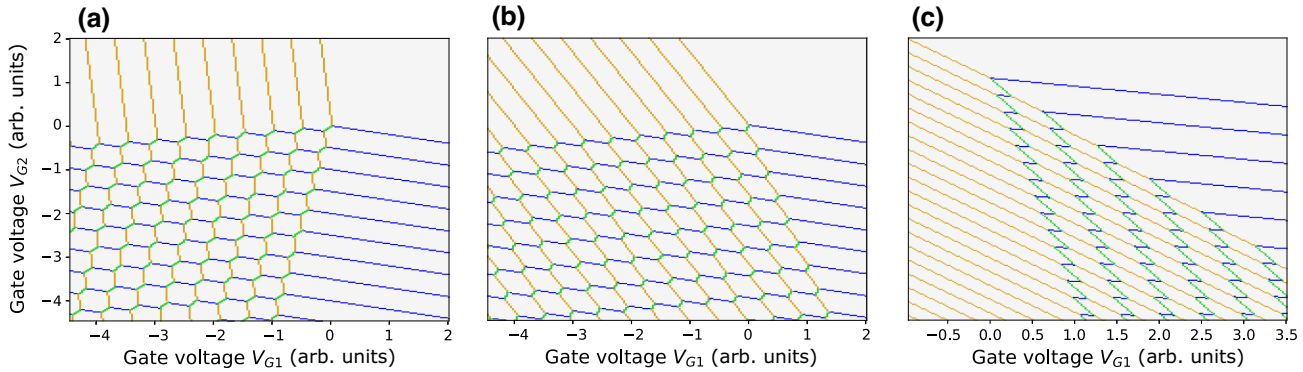

FIG. 6. Diagrams of the dependence of the charge stability on different system parameters. In each charge-stability diagram, G_1 satisfies (violates) inequality (D1) [inequality (D2)]. The charge carriers are assumed to be holes. (a) The regime where D_1 is not loaded via G_2 due to charge occupation in D_2, as inequality (D1) is violated. (b) The regime in which G_2 satisfies both inequalities. (c) Here, G_2 violates inequality (D2), while satisfying inequality (D1).

dot system that better describes a vertically coupled double quantum dot. This should aid the reader in interpreting the experimentally obtained charge-stability diagrams in this paper.

In any double quantum dot system, a particular gate G can only subsequently load a quantum dot D_i if a voltage on G can offset the electrostatic energy arising from the loading of any other quantum dot. In particular, for G to load quantum dots D_1 or D_2 while the other one is occupied, the system has to respectively, satisfy the following inequalities:

$$\frac{E_{C2}}{\alpha_{2,G}} > \frac{E_{Cm}}{\alpha_{1,G}}, \tag{D1}$$

$$\frac{E_{C1}}{\alpha_{1,G}} > \frac{E_{Cm}}{\alpha_{2,G}}. \tag{D2}$$

Here, $\alpha_{1(2),G}$ is the lever arm between the gate G and $D_{1(2)}$, $E_{C1(2)}$ is the charging energy of $D_{1(2)}$, and E_{Cm} is the electrostatic coupling energy [33]. If inequality (D1) [inequality (D2)] is violated, then quantum dot D_1 (D_2) cannot be occupied due to screening from D_2 (D_1).

In planar double quantum dots, each quantum dot is predominantly coupled to a single plunger gate, which in return couples relatively weakly to the other quantum dot. That is, plunger gate G_1 couples predominantly to D_1 such that $\alpha_{1,G_1}/\alpha_{2,G_1} > 1$ and the inequality in Eq. (D1) is satisfied, since $E_{Cm} < E_{C2}$. The same holds for D_2 and the corresponding plunger gate. Figures 6(a) and 6(b) display examples of typical planar double quantum dots hosting holes.

For a vertically coupled double quantum dot, the situation may be different. The lever arm between all gates and the bottom quantum dot can become smaller than to the

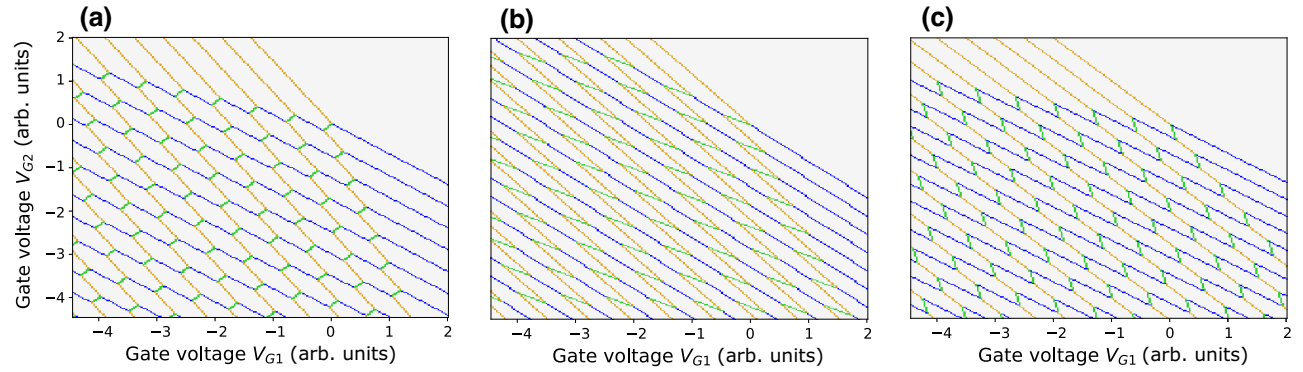

FIG. 7. Charge stability diagrams with different interdot slopes. The interdot slope (depicted in green) depends on the ratio between the lever arms. We denote D_1 (D_2) as the quantum dots with the steep (shallow) reservoir-transition line. A positive interdot slope as in (a) is observed whenever each gate couples predominantly to different quantum dots. If both gates couple more strongly to D_2 than to D_1, the situation in (b) is observed. If both gates couple more to D_1 than to D_2, we observe the situation in (c), as is the case in our experiments. We note that in a real system, the different gate arrangements corresponding to (a)–(c) may also lead to a variation in charging voltage, which has not been highlighted in these simulations.

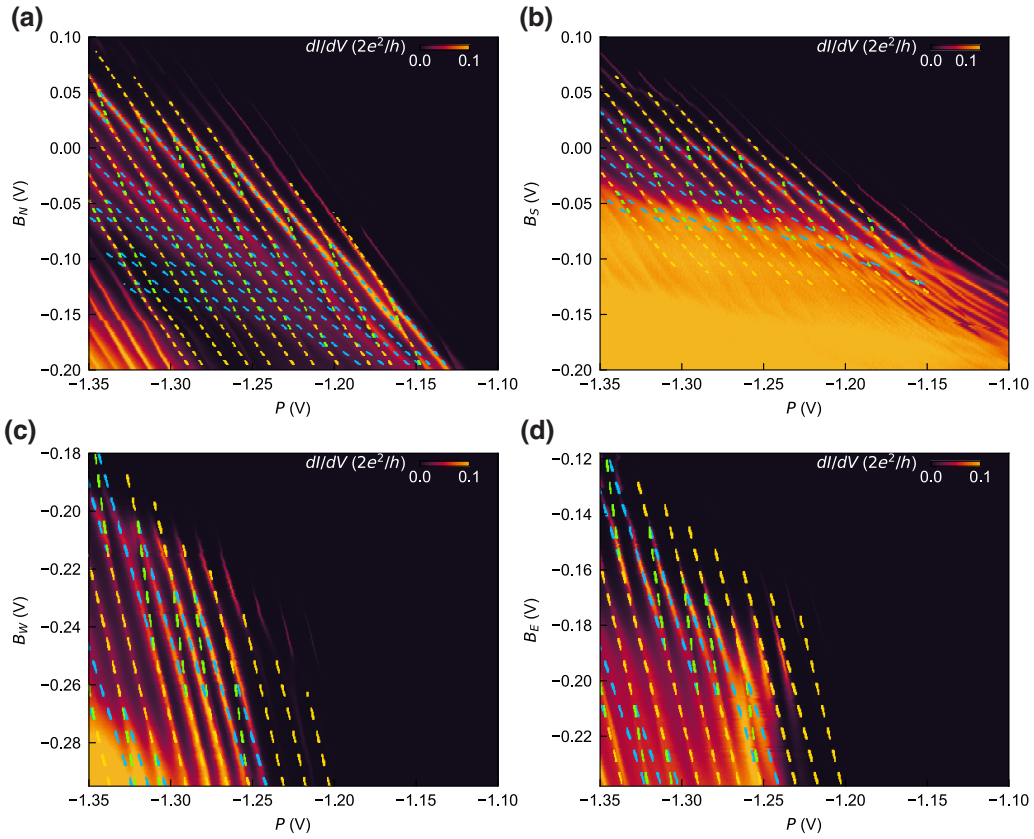

FIG. 8. Charge-stability diagrams as a function of the plunger gate P and the barrier gates B_N, B_S, B_W, and B_E, with electrochemical simulation overlain. A comparison between transport data and the double quantum dot simulation defined by Eq. (E1). The data are measured using lock-in techniques. (a)–(d) The differential conduction through the system as a function of the voltages on the plunger gate P against the voltage applied on (a) B_N, (b) B_S, (c) B_W and (d) B_E. These plots share a common gate reference at $\mathbf{V}_{\text{ref}} = [P = -1.217\,\text{V}, B_N = 0\,\text{V}, B_S = 0\,\text{V}, B_W = -0.237\,\text{V}, B_E = -0.178\,\text{V}]$. The simulation has been limited to the double quantum dot region. Data without the simulation are found in Fig. 9. The code used to produce the simulated transition lines can be found on Zenodo [37].

top quantum dot and the electrostatic coupling energy E_{Cm} is large due to the close proximity of the wave functions. Hence the loading of the top quantum dot might prevent the bottom quantum dot from being loaded, screening the bottom quantum dot. Denoting D_2 as the bottom quantum dot, it is no longer trivial that there is a gate G for which the second inequality is satisfied. Such a situation is depicted in Fig. 6(c). Once D_1 becomes occupied, an increasingly negative voltage on either gate will deplete D_2 instead of loading more holes onto it, making it more challenging to find the desired charge occupation within the operating window of the device.

To ensure loading of the bottom quantum dot, it is therefore crucial to maximize $\alpha_{2,G}/\alpha_{1,G}$ for some gate G. In our experiment, this is achieved by having more in-plane confinement of the top quantum dot, due to the close proximity to the top gates. Less in-plane confinement allows the bottom quantum dot to be more coupled to the surrounding barrier gates. Moreover, the stronger in-plane and out-of-plane confinement of the top quantum dot (D_1) increases the charging energy E_{C1}, making the condition in Eq. (D2) more easily satisfied. We note that in a realistic system, where the lever arms and charging energies are not constant, there could be a transition from one regime to another.

For vertically coupled quantum dots, the interdot transition might also have the opposite slope compared to that of a typical planar double quantum dot. In general, for any double quantum dot system controlled by gates G_1 and G_2, an interdot transition occurs along a line in the voltage space (V_{G1}, V_{G2}) for which

$$\alpha_{1,1}\Delta V_{G1} + \alpha_{1,2}\Delta V_{G2} = \alpha_{2,1}\Delta V_{G1} + \alpha_{2,2}\Delta V_{G2},$$

where $\alpha_{D,G}$ is the lever arm between dot D and gate G and ΔV_G denotes a change in the voltage of gate G. The slope of this line is hence given by

$$\frac{\Delta V_{G2}}{\Delta V_{G1}} = \frac{\alpha_{21} - \alpha_{11}}{\alpha_{12} - \alpha_{22}}.$$

For planar double quantum dots, the plunger gates couple predominantly to different dots, such that $\alpha_{11} > \alpha_{21}$

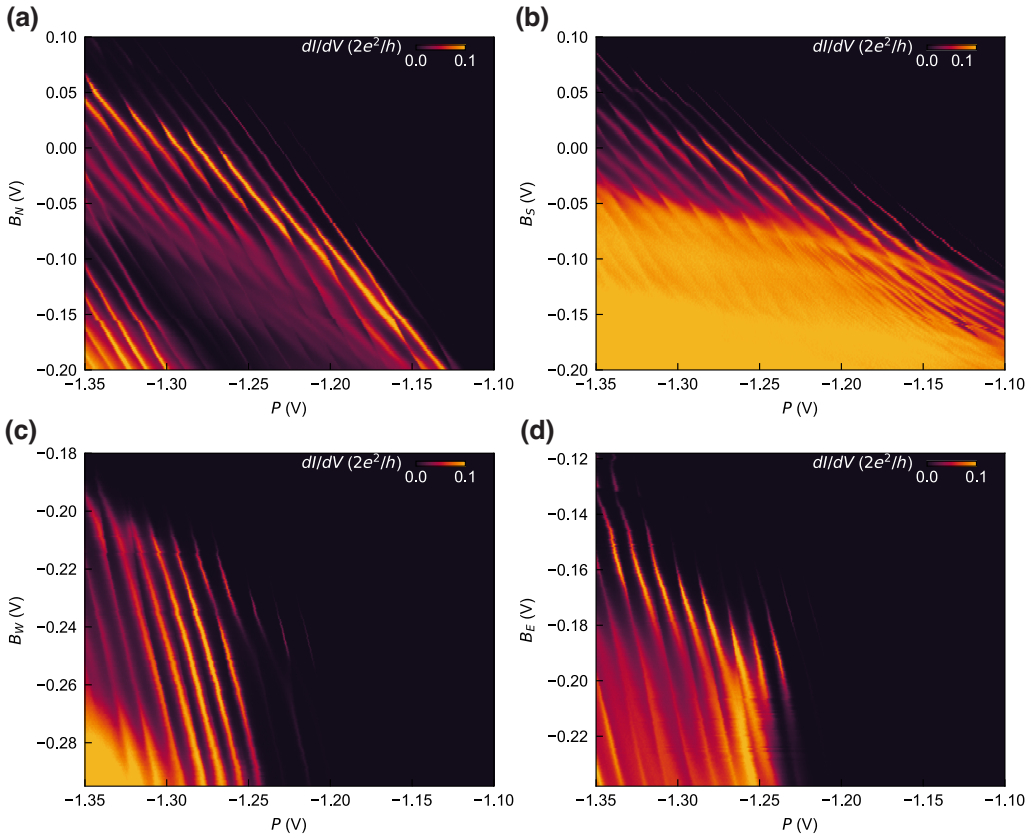

FIG. 9. Charge-stability diagrams as a function of the plunger gate P and the barrier gates B_N, B_S, B_W, and B_E, without electrochemical simulation overlain.

and $\alpha_{22} > \alpha_{12}$. Planar double quantum dots will thus have a positive slope $\Delta V_{G2}/\Delta V_{G1} > 0$ for the interdot transition [Fig. 7(a)]. However, for a vertical double quantum dot, both gates generally couple predominantly to the same dot. This will lead to a negatively sloped interdot transition $\Delta V_{G2}/\Delta V_{G1} < 0$. In our measurements, we observe the situation in Fig. 7(c), suggesting that both gates in our charge-stability diagrams are dominantly coupled to the same quantum dot located in the upper quantum well. This also suggests that loading of the bottom dot is only possible due to the large charging energy of the top quantum dot, compared to the mutual electrostatic interaction.

APPENDIX E: COMPARISON BETWEEN MEASURED CHARGE STABILITY DIAGRAMS AND ELECTROCHEMICAL SIMULATION

In order to extract the lever-arm ratios of both quantum dots as described in the main text, charge-stability diagrams (CSDs) were measured by varying the plunger gate voltage P together with the voltage of surrounding barrier gates (Fig. 8). The interdot transitions in these measurements are less pronounced compared to Fig. 2, this being attributed to a change in the tunnel coupling due to a different voltage regime. In this appendix, we compare these measurements with classical electrochemical simulations of a double quantum dot system [33].

The charge carriers in the simulation are holes and gates couple to both quantum dots through the occupation-dependent lever-arm matrix α. Hence the electrochemical potential μ of the quantum dots is given by

$$\begin{aligned}\mu_1(N_1,N_2,\mathbf{V}) &= \Sigma_{n_1=1}^{N_1} E_{C1}(n_1) + \Sigma_{n_2=1}^{N_2} E_{Cm}(N_1,n_2) \\ &\quad + \alpha_1(N_1,N_2,\mathbf{V})\mathbf{V}, \\ \mu_2(N_1,N_2,\mathbf{V}) &= \Sigma_{n_2=1}^{N_2} E_{C2}(n_2) + \Sigma_{n_1=1}^{N_1} E_{Cm}(n_1,N_2) \\ &\quad + \alpha_2(N_1,N_2,\mathbf{V})\mathbf{V},\end{aligned} \tag{E1}$$

where $N_{1(2)}$ denotes the occupation of the top (bottom) quantum dot, $E_{C1(2)}(N_{1(2)})$ and $E_{Cm}(N_1,N_2)$ are the occupation-dependent charging energies of the top (bottom) quantum dot and the electrostatic interdot coupling energy, respectively, and $\mathbf{V}$ is the vector denoting the gate voltages. The coupling between the gates and the top (bottom) quantum dot is given by two row matrices $\alpha_{1(2)}$, with purely positive entries. These lever arms are generally taken to be occupation and voltage dependent. Since the charging energy is poorly defined for level-dependent lever

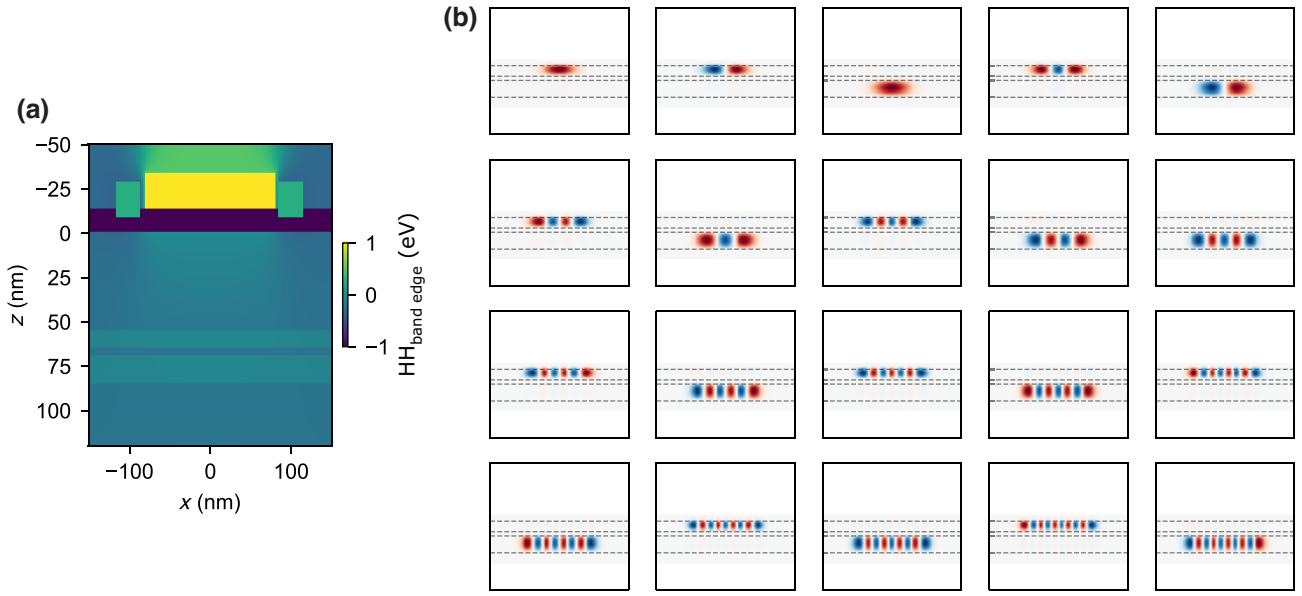

FIG. 10. The results of the 2D Schrödinger-Poisson simulations. (a) The HH band edge as a function of the x and z coordinates for the bilayer heterostructure, which also comprises the gate stack for $z < 0$, where z is the growth direction. (b) A color map of the wave-function amplitude for the first 20 energy levels ordered from left to right, top to bottom.

arms, these are defined at an (arbitrary) fixed reference voltage $\mathbf{V}_{\text{ref}}$:

$$E_{C1(2)}(N_{1(2)}) \equiv \mu_{1(2)}(N_{1(2)}, N_{2(1)}, \mathbf{V}_{\text{ref}}) - \mu_{1(2)}(N_{1(2)} - 1, N_{2(1)}, \mathbf{V}_{\text{ref}}), \quad \text{(E2)}$$

fixing $\mu(0, 0, \mathbf{V}_{\text{ref}}) = 0$. The charging energies and the interdot capacitive energies are consistent across the simulations in Fig. 8. To reduce the free parameters further, the coupling matrix α is simplified. $\alpha_1(V_P)$ and $\alpha_2(N_2, V_P)$ are dependent on the plunger gate voltage V_P, instead of on all the gate voltages, with the latter also depending on the occupation of the bottom quantum dot. With these assumptions, the data match a charge-stability diagram of a double quantum dot as seen in Figs. 8 and 2. The parameters used can be found in full on Zenodo [37]. This match suggests that the system indeed consists of a double quantum dot, with no additional dot interacting with it in a meaningful way. The latter would namely result in additional (triangular, pentagonal, or heptagonal) features that we do not observe.

To achieve the observed match, the lever arms between the gates and the bottom quantum dot need a significant dependency on the occupation of the bottom quantum dot. This is not as pronounced for the top quantum dot, which is expected from the stronger in-plane confinement. Any additional charges on the top quantum dot will have a larger impact on its size and thus on the coupling to the barrier gates.

We note that the plunger gate voltage has a significant effect on the lever arm of B_S, as seen by the curvature of the transition lines in Fig. 9(b). This suggests that the plunger gate significantly changes the capacitive coupling between B_S and the quantum dots, which would occur if the quantum dots are close to B_S. This is consistent with the estimated positions of the quantum dots that are presented in the main text.

Small discrepancies between the data and the electrochemical simulation are attributed to the limited parameters of the model, such as the neglected dependence on the top quantum dot occupation and the exclusion of tunnel coupling. Moreover, for increasingly negative voltages on B_N and B_S, the system is generally poorly described by a double quantum dot, as seen in Figs. 8(a) and 8(b). For lower voltages on B_N (and P), the overall transport first decreases, which we attribute to the same phenomenon that leads to the decrease in the Coulomb peak amplitude in Fig. 1(c) (lower panel), namely, a larger tunnel coupling between the top and bottom layers. This increased tunnel coupling could change the interaction between the quantum dots and the leads. At even lower voltages B_N and P, a single-dot charge-stability diagram emerges corresponding to loading of the top quantum dot, which corresponds to either the merging of the top and bottom quantum dot or the screening of the bottom quantum dot by the top layer. For the latter case, the possibility of this transition is described in Appendix D. For lower voltages on B_S, we observe a large background current [Fig. 8(b)]. This background current seems to emerge as the resonances of one of the quantum dots become poorly defined and closely spaced. We propose that a conductive channel is formed under B_S through one of the layers of the quantum well.

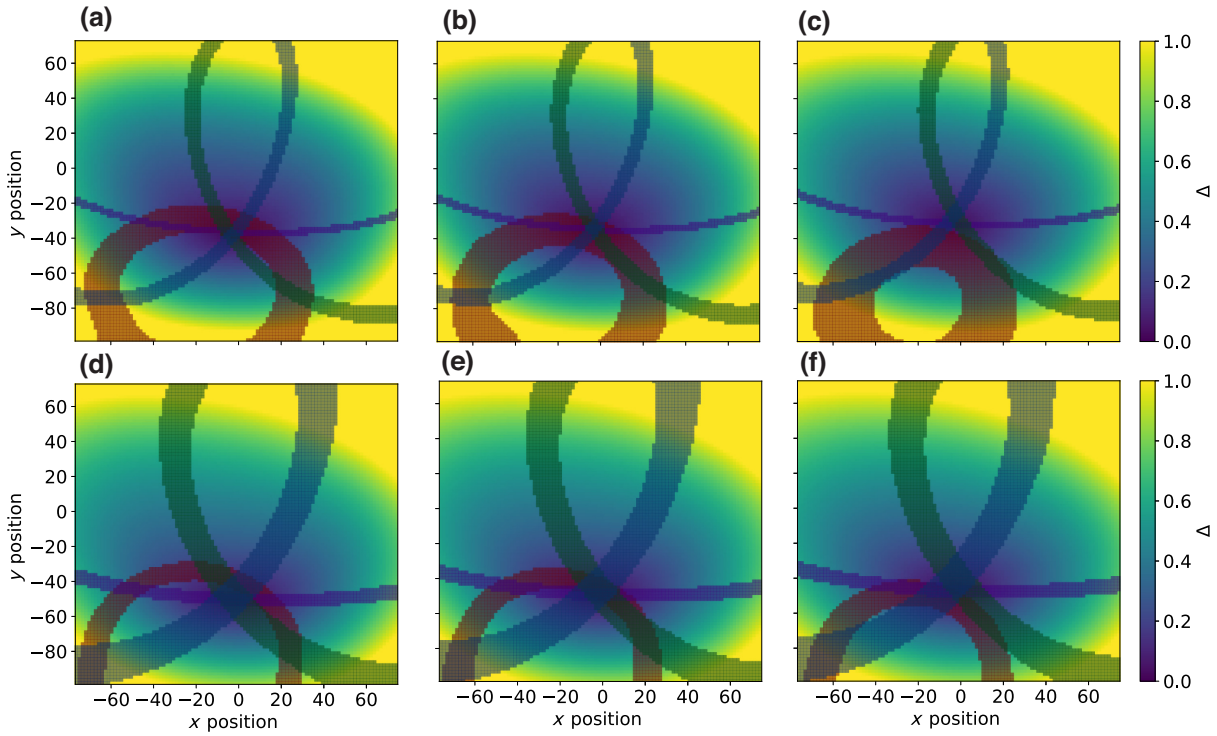

FIG. 11. Triangulation of the quantum dots. Within the red, purple, green, and blue contours, the simulated lever arm to the respective gate is within the standard deviation of the empirically extracted values. For D_{top}, these are $\tilde{\alpha}_{B_N,\text{meas}} = 0.44 \pm 0.02$, $\tilde{\alpha}_{B_S,\text{meas}} = 0.53 \pm 0.02$, $\tilde{\alpha}_{B_W,\text{meas}} = 0.41 \pm 0.02$, and $\tilde{\alpha}_{B_E,\text{meas}} = 0.40 \pm 0.02$, respectively. For D_{bot}, they are $\tilde{\alpha}_{B_N,\text{meas}} = 0.55 \pm 0.01$, $\tilde{\alpha}_{B_S,\text{meas}} = 0.76 \pm 0.04$, $\tilde{\alpha}_{B_W,\text{meas}} = 0.53 \pm 0.04$, and $\tilde{\alpha}_{B_E,\text{meas}} = 0.53 \pm 0.05$, respectively. The measurement and simulation agree best at the position for which Δ is minimal. The origin is defined at the center of the plunger gate. (a)–(c) The results for D_{top}, simulated in the top quantum well, for radii of (a) 20, (b) 30, and (c) 40 nm. (d)–(f) Similarly, the results for D_{bot}, as it is simulated in the bottom quantum well, for radii of (d) 20, (e) 30, and (f) 40 nm. For both quantum dots, other radii and simulation within the other quantum well result in a higher minimal Δ.

Despite these discrepancies, the good match between the data and this relatively simple model strongly supports the assertion that the system in question consists of a double quantum dot without any additional quantum dots.

The code and the parameters used to perform the simulation can be found in full on Zenodo [37]. Here, the parameters to fit the charge-stability diagram in Fig. 2 are also found.

APPENDIX F: SCHRÖDINGER-POISSON SIMULATION

We perform 2D Schrödinger-Poisson simulation with the NEXTNANO software package [38]. Figure 10(a) shows the heavy-hole (HH) band edge for the heterostructure ($z > 0$) where the top edges of the quantum wells are positioned at $z = 55$ nm and $z = 69$ nm. For $z < 0$, the gate stack is visible. This comprises a plunger gate, two barrier gates, and a layer of Al_2O_3. Figure 10(b) shows the wavefunction amplitude for the first 20 2D orbitals for which we have calculated the lever arm. The potentials applied to the plunger and the barriers are -1.15 V and -0.25 V, respectively.

We estimate the tunnel coupling between the two quantum wells by solving the Schrödinger equation for this system and extracting the symmetric to antisymmetric gap between the first two energy states, from which we obtain $t_c^{QW} = 16$ GHz. Assuming a harmonic confinement potential in the in-plane direction and the dot center in the same axis, the single-hole dot-dot tunnel coupling can then be obtained from the radii of the two dots (r_{top} and r_{bottom}) as $t_c^{QD} = t_c^{QW}(2r_1r_2)/(r_1^2 + r_2^2)$, where r is the Bohr radius. From these assumptions, the upper bound on the estimated dot-dot tunnel coupling for the case of equally sized quantum dots is $t_c^{QD} = t_c^{QW} = 16$ GHz.

APPENDIX G: FINITE-ELEMENT SIMULATIONS OF CAPACITANCE

To get an indication of the position of the quantum dots based on the lever arms, a finite-element simulation with ANSYS Q3D [36] has been performed, to extract the geometric capacitance between a gate and a quantum dot. These simulated geometric capacitances are converted to

TABLE I. The relative dielectric permittivity used in the ANSYS simulation. For the properties of $Si_{0.2}Ge_{0.8}$, a linear approximation based on the atomic concentration is used.

Material	ϵ_r
Al_2O_3 [39]	5.9
Ge [40]	15.8
$Si_{0.2}Ge_{0.8}$ [40]	15.0
SiO_2 [41]	3.9

lever-arm ratios by dividing the absolute quantum dot-barrier gate capacitance by the quantum dot-plunger gate capacitance. The simulated lever-arm ratios are then compared to those obtained from the charge-stability diagrams and the position at which these best match each other is determined (see Fig. 11). This is simulated for the quantum dot being positioned in either the top or the bottom well. The heterostructure has been modeled up to 500 nm in plane around the plunger gate and up to a depth of 125 nm below the bottom quantum well. The reservoirs underneath the Ohmic gates are excluded in this simulation. While these gates may affect the electrostatic coupling of the other gates to the quantum dot, their symmetric positioning will partly compensate for their impact on the quantum dot location. The dielectric material permittivities used in the simulation can be found in Table I. The metallic gates have been simulated as uniform perfect conductors.

To emulate a quantum dot, a circular perfectly conducting uniform disk is placed in either quantum well. This allows us to estimate the geometric capacitance between the quantum dot and the surrounding gates. Each quantum dot is simulated with different disk radii. We note that the wave-function density of the quantum dot is not taken into account here and noncircular shapes are not investigated.

To determine how well the simulations fit the experimental data, we determine the Euclidean distance $\Delta = \sqrt{\sum_{B_i}(\tilde{\alpha}_{B_i,\mathrm{meas}} - \tilde{\alpha}_{B_i,\mathrm{sim}})^2}$, where $\tilde{\alpha}_{B_i,\mathrm{meas(sim)}}$ is the measured (simulated) lever-arm ratio α_{B_i}/α_P and the sum is taken over the barrier gates B_N, B_S, B_E, and B_W. This Δ is the cost-metric from which we estimate the position (and approximate radius) of the quantum dot.

For each analyzed quantum dot and quantum well, there is a particular position and radius at which Δ is minimized (see Fig. 11). These are considered to be the most probable locations and radii of that particular quantum dot in the quantum well.

To achieve the minimal Δ, the quantum dots are both predicted to have a radius of about 30 nm and are positioned closer than that to each other (Fig. 12). The radius determined here is lower than expected from the plunger gate size, with the discrepancy arising from the approximation of the quantum dot as a uniform disk. From their proximity, we conclude that the quantum dots are likely to be in two separate wells. Δ is minimized for D_{top} whenever it is located in the top well and for D_{bot} when it is in the bottom well. This is consistent with the allocation made in the main text.

Future improvements on this method would consider the electrostatic potential arising from the gates, the strain of the system, and the effects of the disorder. Moreover, the interplay between multiple quantum dots spread across the wells can be taken into account in the future, as we stress that currently just a single quantum dot is simulated at a

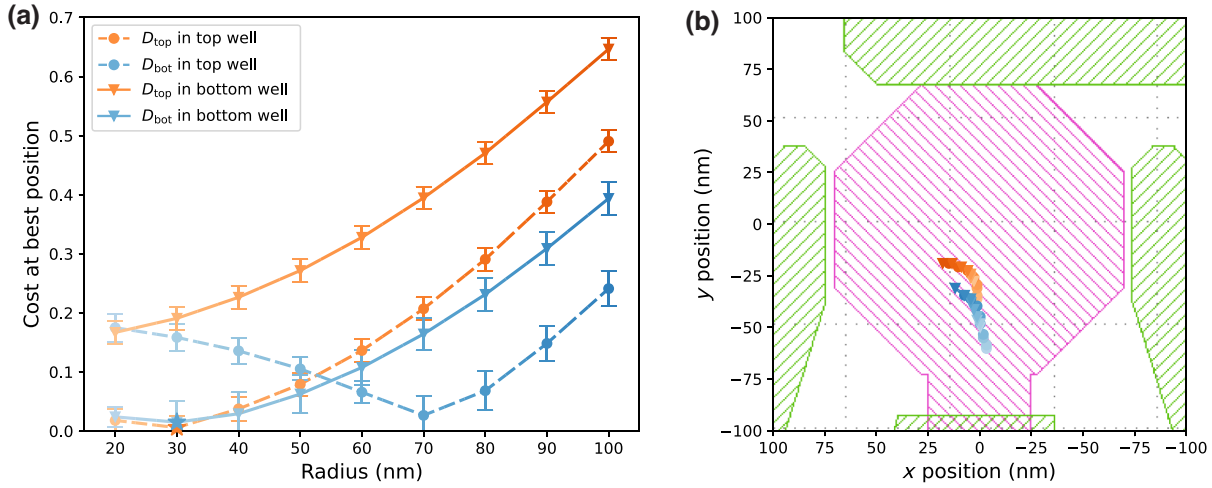

FIG. 12. The simulated quantum dot radius and position. (a) The Δ corresponding to the most likely quantum dot position for a given quantum dot radius. The simulation and experiments have been compared for either quantum dot in both wells. Quantum dot 1 (2) corresponds to the orange (blue) transitions in Fig. 2. For each quantum dot, the most likely radius is 30 nm. The error bars are based on the standard deviation in the slopes extracted from the raw data in Fig. 8. (b) The expected position for each radius of the two quantum dots in either the bottom or the top well. For all radii, the quantum dots are close to one another. The darker colors correspond to the larger radii as depicted in (a).

time. A self-consistent 3D Schrödinger-Poisson approach could make this possible.

[1] S. G. J. Philips, M. T. Mądzik, S. V. Amitonov, S. L. de Snoo, M. Russ, N. Kalhor, C. Volk, W. I. L. Lawrie, D. Brousse, L. Tryputen, B. P. Wuetz, A. Sammak, M. Veldhorst, G. Scappucci, and L. M. K. Vandersypen, Universal control of a six-qubit quantum processor in silicon, Nature **609**, 919 (2022).

[2] N. W. Hendrickx, W. I. L. Lawrie, M. Russ, F. van Riggelen, S. L. de Snoo, R. N. Schouten, A. Sammak, G. Scappucci, and M. Veldhorst, A four-qubit germanium quantum processor, Nature **591**, 580 (2021).

[3] P. Stano and D. Loss, Review of performance metrics of spin qubits in gated semiconducting nanostructures, Nat. Rev. Phys. **4**, 672 (2021).

[4] J. Yoneda, K. Takeda, T. Otsuka, T. Nakajima, M. R. Delbecq, G. Allison, T. Honda, T. Kodera, S. Oda, Y. Hoshi, N. Usami, K. M. Itoh, and S. Tarucha, A quantum-dot spin qubit with coherence limited by charge noise and fidelity higher than 99.9%, Nat. Nanotechnol. **13**, 102 (2018).

[5] W. I. L. Lawrie, M. Rimbach-Russ, F. van Riggelen, N. W. Hendrickx, S. L. de Snoo, A. Sammak, G. Scappucci, J. Helsen, and M. Veldhorst, Simultaneous single-qubit driving of semiconductor spin qubits at the fault-tolerant threshold, Nat. Commun. **14**, 3617 (2023).

[6] X. Xue, M. Russ, N. Samkharadze, B. Undseth, A. Sammak, G. Scappucci, and L. M. K. Vandersypen, Quantum logic with spin qubits crossing the surface code threshold, Nature **601**, 343 (2022).

[7] A. Noiri, K. Takeda, T. Nakajima, T. Kobayashi, A. Sammak, G. Scappucci, and S. Tarucha, Fast universal quantum gate above the fault-tolerance threshold in silicon, Nature **601**, 338 (2022).

[8] K. Takeda, A. Noiri, T. Nakajima, T. Kobayashi, and S. Tarucha, Quantum error correction with silicon spin qubits, Nature **608**, 682 (2022).

[9] F. van Riggelen, W. I. L. Lawrie, M. Russ, N. W. Hendrickx, A. Sammak, M. Rispler, B. M. Terhal, G. Scappucci, and M. Veldhorst, Phase flip code with semiconductor spin qubits, npj Quantum Inf. **8**, 124 (2022).

[10] F. Borsoi, N. W. Hendrickx, V. John, M. Meyer, S. Motz, F. van Riggelen, A. Sammak, S. L. de Snoo, G. Scappucci, and M. Veldhorst, Shared control of a 16 semiconductor quantum dot crossbar array, Nat. Nanotechnol. (2023).

[11] L. M. K. Vandersypen, H. Bluhm, J. S. Clarke, A. S. Dzurak, R. Ishihara, A. Morello, D. J. Reilly, L. R. Schreiber, and M. Veldhorst, Interfacing spin qubits in quantum dots and donors—hot, dense, and coherent, npj Quantum Inf. **3**, 34 (2017).

[12] Z. Wang, M. Feng, S. Serrano, W. Gilbert, R. C. C. Leon, T. Tanttu, P. Mai, D. Liang, J. Y. Huang, Y. Su, W. H. Lim, F. E. Hudson, C. C. Escott, A. Morello, C. H. Yang, A. S. Dzurak, A. Saraiva, and A. Laucht, Jellybean quantum dots in silicon for qubit coupling and on-chip quantum chemistry, Adv. Mater. **35**, 2208557 (2023).

[13] F. Borjans, X. G. Croot, X. Mi, M. J. Gullans, and J. R. Petta, Resonant microwave-mediated interactions between distant electron spins, Nature **577**, 195 (2020).

[14] J. Yoneda, W. Huang, M. Feng, C. H. Yang, K. W. Chan, T. Tanttu, W. Gilbert, R. C. C. Leon, F. E. Hudson, K. M. Itoh, A. Morello, S. D. Bartlett, A. Laucht, A. Saraiva, and A. S. Dzurak, Coherent spin qubit transport in silicon, Nat. Commun. **12**, 4114 (2021).

[15] A. Tosato, B. Ferrari, A. Sammak, A. R. Hamilton, M. Veldhorst, M. Virgilio, and G. Scappucci, A high-mobility hole bilayer in a germanium double quantum well, Adv. Quantum Technol. **5**, 2100167 (2022).

[16] D. Laroche, S.-H. Huang, E. Nielsen, C. W. Liu, J.-Y. Li, and T. M. Lu, Magneto-transport of an electron bilayer system in an undoped Si/SiGe double-quantum-well heterostructure, Appl. Phys. Lett. **106**, 143503 (2015).

[17] M. G. Borselli, R. S. Ross, A. A. Kiselev, E. T. Croke, K. S. Holabird, P. W. Deelman, L. D. Warren, I. Alvarado-Rodriguez, I. Milosavljevic, F. C. Ku, W. S. Wong, A. E. Schmitz, M. Sokolich, M. F. Gyure, and A. T. Hunter, Measurement of valley splitting in high-symmetry Si/SiGe quantum dots, Appl. Phys. Lett. **98**, 123118 (2011).

[18] F. van Riggelen-Doelman, C.-A. Wang, S. L. de Snoo, W. I. L. Lawrie, N. W. Hendrickx, M. Rimbach-Russ, A. Sammak, G. Scappucci, C. Déprez, and M. Veldhorst, Coherent spin qubit shuttling through germanium quantum dots, ArXiv:2308.02406 (2023).

[19] T. Fujita, T. A. Baart, C. Reichl, W. Wegscheider, and L. M. K. Vandersypen, Coherent shuttle of electron-spin states, npj Quantum Inf. **3**, 22 (2017).

[20] P. M. Mutter and G. Burkard, Natural heavy-hole flopping mode qubit in germanium, Phys. Rev. Res. **3**, 13194 (2021).

[21] H. Malissa, D. Gruber, D. Pachinger, F. Schäffler, W. Jantsch, and Z. Wilamowski, Design and fabrication of a sige double quantum well structure for *g*-factor tuning, Superlattices Microstruct. **39**, 414 (2006).

[22] G. Scappucci, C. Kloeffel, F. A. Zwanenburg, D. Loss, M. Myronov, J. J. Zhang, S. De Franceschi, G. Katsaros, and M. Veldhorst, The germanium quantum information route, Nat. Rev. Mater. **6**, 926 (2020).

[23] R. Vrijen, E. Yablonovitch, K. Wang, H. W. Jiang, A. Balandin, V. Roychowdhury, T. Mor, and D. DiVincenzo, Electron-spin-resonance transistors for quantum computing in silicon-germanium heterostructures, Phys. Rev. A **62**, 012306 (2000).

[24] C.-A. Wang, C. Déprez, H. Tidjani, W. I. L. Lawrie, N. W. Hendrickx, A. Sammak, G. Scappucci, and M. Veldhorst, Probing resonating valence bonds on a programmable germanium quantum simulator, npj Quantum Inf. **9**, 58 (2023).

[25] S. Conti, S. Saberi-Pouya, A. Perali, M. Virgilio, F. M. Peeters, A. R. Hamilton, G. Scappucci, and D. Neilson, Electron–hole superfluidity in strained Si/Ge type II heterojunctions, npj Quantum Mater. **6**, 41 (2021).

[26] D. Nandi, A. D. K. Finck, J. P. Eisenstein, L. N. Pfeiffer, and K. W. West, Exciton condensation and perfect Coulomb drag, Nature **488**, 481 (2012).

[27] R. Wang, T. Sedrakyan, B. Wang, D. Lingjie, and D. Rui-Rui, Excitonic topological order in imbalanced electron-hole bilayers, Nature **619**, 57 (2023).

[28] D. Buterakos and S. D. Sarma, Magnetic phases of bilayer quantum-dot Hubbard model plaquettes, ArXiv:2308.04504 (2023).

[29] A. Hamo, A. Benyamini, I. Shapir, I. Khivrich, J. Waissman, K. Kaasbjerg, Y. Oreg, F. von Oppen, and S. Ilani, Electron attraction mediated by coulomb repulsion, Nature **535**, 395 (2016).

[30] C. Hong, G. Yoo, J. Park, M.-K. Cho, Y. Chung, H.-S. Sim, D. Kim, H. Choi, V. Umansky, and D. Mahalu, Attractive Coulomb interactions in a triple quantum dot, Phys. Rev. B **97**, 241115 (2018).

[31] A. R. Hamilton, E. H. Linfield, M. J. Kelly, D. A. Ritchie, G. A. Jones, and M. Pepper, Transition from one- to two-subband occupancy in the 2DEG of back-gated modulation-doped GaAs-GaAl$_{x1-x}$As heterostructures, Phys. Rev. B **51**, 17600 (1995).

[32] D. Y. Baines, T. Meunier, D. Mailly, A. D. Wieck, C. Bäuerle, L. Saminadayar, P. S. Cornaglia, G. Usaj, C. A. Balseiro, and D. Feinberg, Transport through side-coupled double quantum dots: From weak to strong interdot coupling, Phys. Rev. B **85**, 195117 (2012).

[33] W. G. van der Wiel, S. De Franceschi, J. M. Elzerman, T. Fujisawa, S. Tarucha, and L. P. Kouwenhoven, Electron transport through double quantum dots, Rev. Mod. Phys. **75**, 1 (2002).

[34] S. D. Franceschi, S. Sasaki, J. M. Elzerman, W. G. van der Wiel, S. Tarucha, and L. P. Kouwenhoven, Electron cotunneling in a semiconductor quantum dot, Phys. Rev. Lett. **86**, 878 (2001).

[35] D. Schröer, A. D. Greentree, L. Gaudreau, K. Eberl, L. C. L. Hollenberg, J. P. Kotthaus, and S. Ludwig, Electrostatically defined serial triple quantum dot charged with few electrons, Phys. Rev. B **76**, 075306 (2007).

[36] ANSYS® Electronics Desktop, Release 22.2 (2022).

[37] https://zenodo.org/record/8316529

[38] S. Birner, T. Zibold, T. Andlauer, T. Kubis, M. Sabathil, A. Trellakis, and P. Vogl, Nextnano: General purpose 3-D simulations, IEEE Trans. Electron Devices **54**, 2137 (2007).

[39] M. Groner, J. Elam, F. Fabreguette, and S. George, Electrical characterization of thin Al_2O_3 films grown by atomic layer deposition on silicon and various metal substrates, Thin Solid Films **413**, 186 (2002).

[40] W. C. Dunlap and R. L. Watters, Direct measurement of the dielectric constants of silicon and germanium, Phys. Rev. **92**, 1396 (1953).

[41] S. M. Sze, *Physics of Semiconductor Devices* (Wiley, New York, 1981).